JOURNAL OF GEOPHYSICAL RESEARCH, VOL. 115, A02201, doi:10.1029/2009JA014709, 2010

On the origin of high *m* magnetospheric waves

M. Beharrell,[1] A. J. Kavanagh,[1] and F. Honary[1]

Received 29 July 2009; revised 17 September 2009; accepted 20 October 2009; published 3 February 2010.

[1] A survey of Advanced Rio-Imaging Experiment in Scandinavia data reveals evidence for a previously overlooked generation mechanism of high azimuthal wave number magnetospheric waves. Here we present observations of pulsating cosmic noise absorption with azimuthal wave numbers as high as 380, suggestive of precipitation modulation by magnetospheric waves. Dispersion relations of the small-scale precipitation pulsations are indicative of the proposed origin. Previous studies of magnetospheric waves, together with data from the Charge And Mass Magnetospheric Ion Composition Experiment (Magnetospheric Ion Composition Sensor) instrument aboard the Polar spacecraft, provide support for the theory.

Citation: Beharrell, M., A. J. Kavanagh, and F. Honary (2010), On the origin of high *m* magnetospheric waves, *J. Geophys. Res.*, *115*, A02201, doi:10.1029/2009JA014709.

1. Introduction

[2] Pulsations in the precipitation of energetic electrons (>30 keV) have long been observed in cosmic noise absorption (CNA). These pulsations often appear in the measurements of relative ionospheric opacity meters (riometers) and are generally linked to the occurrence of standing magnetospheric Alfvén waves, known as field line resonances (FLR) [e.g., *Spanswick et al.*, 2005]. This is not the sole source of these pulsations; *Senior and Honary* [2003] identified a westward propagating wave in the Imaging Riometer for Ionospheric Studies (IRIS), which they attributed to modulation via a drift or drift-bounce resonant wave.

[3] The variations in *D* region electron densities caused by precipitating electron pulsations have also been observed with ionospheric radar. *Yeoman and Wright* [2000] conducted a detailed case study of an event on 18 October 1999, with the CUTLASS HF radars. Three distinct waves were identified. The first had a large-scale nature, suggesting a driving source external to the magnetosphere, whereas the second and third had smaller azimuthal scale lengths, suggestive of an internal driving mechanism.

[4] Occurring almost exclusively during the morning and early afternoon, eastward propagating waves with high azimuthal wave numbers are an interesting, yet common, subset of CNA pulsation.

[5] *Kikuchi* [1988] used a scanning beam riometer to measure the period and velocity of 19 such waves. He reported that this newly discovered type of pulsation occurred between 5 and 10 magnetic local time (MLT) and had a short azimuthal wavelength, corresponding to an *m* number of 20–180. The eastward direction led him to conclude "the primary source must be located in the nightside magnetosphere."

[6] It is possible to classify magnetospheric ULF waves according to their mode of propagation. Shear Alfvén waves propagate along field lines, reflected by the high conductivity ionosphere in the northern and southern hemispheres, whereas compressional fast mode waves propagate perpendicular to the magnetic field, reflected by the low latitude ionosphere and an outer boundary, usually taken to be the magnetopause.

[7] Standing waves of each type resonate at eigenfrequencies dependent on the wave speed and the length of the field line or size of the cavity. The theory of standing Alfvén waves, or field line resonance, is well known and has been used extensively to explain geomagnetic pulsation observations and to infer plasma density along field lines.

[8] It is accepted that cavity modes excite toroidal Alfvén waves, with particularly strong coupling where the compressional wave frequency matches the natural resonance of the field line. This is an important process in the generation mechanism we propose for high *m* number waves, and in section 3.2 we employ a simple box model of the dayside magnetosphere to help qualitatively describe the coupling. Toroidal Alfvén modes are capable of energy exchange with the magnetospheric charged particle population, through Landau and inverse-Landau damping of particles close to drift-bounce resonance.

[9] The Advanced Rio-Imaging Experiment in Scandinavia (ARIES) is a new type of imaging riometer with a spatial resolution of less than 10 km at zenith and over 500 individual beams. It has provided the greatest imaging resolution of any riometer to date and facilitated the identification of a large number of high *m* number waves within a single 6-month period.

[10] For the first time, a complete generating mechanism for these waves is described, beginning with a source external to the magnetosphere and ultimately resulting in the observed structured cosmic noise absorption. Inferred cavity

[1]Department of Communication Systems, University of Lancaster, Lancaster, UK.

0148-0227/10/2009JA014709$09.00

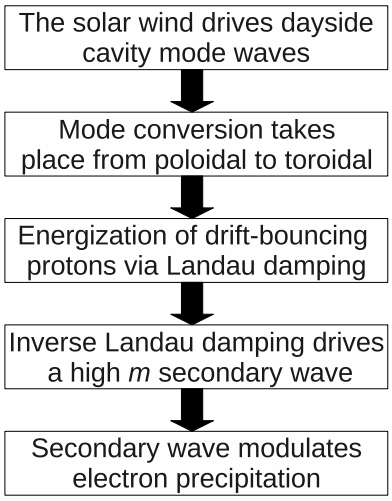

Figure 1. An overview of the proposed generation mechanism.

modes are found to match established frequencies, and the results are tested with data from a polar orbiting satellite to determine whether appropriate positive gradient regions exist in the energy distribution of drift-bouncing ions.

2. Instruments

2.1. ARIES

[11] ARIES [*Grill et al.*, 2003] was the first of its kind, a relative ionospheric opacity meter (riometer) based around a Mills Cross antenna array. This configuration achieves a fourfold increase in spacial resolution when compared with other imaging riometers with the same number of antennas. ARIES receives at 38.2 MHz and uses a Field Programmable Gate Array (FPGA) to conduct beam forming entirely in the digital domain. The angular resolution reaches a maximum of 4.75° at zenith. It is located near Ramfjordmoen, Norway (69.63°N, 19.52°E).

2.2. CAMMICE (POLAR)

[12] The Charge And Mass Magnetospheric Ion Composition Experiment (CAMMICE), aboard the Polar spacecraft [*Acuña et al.*, 1995], provided energetic particle composition data from two instruments. The data set utilized in this study is from the Double Coincidence Rate (DCR) channel of the Magnetospheric Ion Composition Sensor (MICS) [*Wilken et al.*, 1992]. The DCR channel responded mainly to the dominant proton species, with energy bins spaced logarithmically between 1 and 328 keV and a spin averaged temporal resolution of 192 s. Prior to its end of life in 2008, Polar was in a 1.8 × 9 R_E polar orbit, with an ≈86° inclination to the equator. Its spin was stabilized perpendicular to the orbital plane, with a period of 6 s.

3. Theory

3.1. Generation Mechanism Overview

[13] We propose a generation mechanism of high azimuthal wave number waves, which can be broken down into five steps as shown in Figure 1.

[14] Solar wind pressure pulses on the dayside magnetopause excite quantized standing waves in the magnetospheric cavity. These compressional modes couple to toroidal Alfvén field line oscillations, which share the low azimuthal wave numbers of the cavity modes.

[15] Drift-bouncing magnetospheric protons are accelerated by the toroidal waves though Landau damping, causing a bump to appear on the tail of the proton energy distribution. Following a reduction of the initial driving wave, this free energy becomes unstable to inverse-Landau damping, and a secondary toroidal wave is generated.

[16] The energy of a proton in resonance with a wave is determined by both the frequency and the azimuthal wave number of the wave. As a consequence, secondary waves take a range of frequencies and azimuthal wave numbers, while obeying a dispersion relation determined by the proton energy. Distinctive, high azimuthal wave numbers are often observed.

[17] By modulating the growth of whistler mode waves and, subsequently, the pitch angle scattering of electrons into the loss cone [*Coroniti and Kennel*, 1970], images of these ULF waves appear in the cosmic noise absorption measured by riometers.

3.2. Magnetospheric Cavity Modes

[18] To describe the magnetospheric cavity modes and coupled field line resonances, we follow the method of *Cheng et al.* [1998] by solving the linearized ideal MHD wave equation in simple Cartesian coordinates. X represents the radial distance and Y the azimuthal distance, with positive Y toward dusk. The Z direction follows the magnetic field, from the South to the North Pole:

$$\frac{d^2\mathbf{E}_1}{dt^2} = \frac{1}{\mu_0\rho_0} \cdot [(\nabla\times\nabla\times\mathbf{E_1})\times\mathbf{B_0}\times\mathbf{B_0} + (\nabla\times\mathbf{B_0})\times(\nabla\times\mathbf{E_1})\times\mathbf{B_0}], \quad (1)$$

where $\mathbf{B_0}$ is the ambient magnetic field, ρ_0 the ambient plasma density, and $\mathbf{E_1}$ the electric field perturbation.

[19] In ideal MHD there is no electric field component along the magnetic field. $\mathbf{E_1}$ may therefore be described by

$$\mathbf{E_1} = (E_{1X}(X), E_{1Y}(X), 0)\cdot\exp[i(k_Y Y + k_Z Z - \omega t)], \quad (2)$$

where k_Y and k_Z are the wave numbers in the Y and Z directions, respectively.

[20] In order to explore standing wave modes, equation (1) is decomposed into two steady state differential equations: the first to be solved for E_{1Y} and the second giving E_{1X}:

$$\frac{d^2E_{1Y}}{dX^2} + \left\{\frac{2k_Y^2\omega^2\left(\frac{dv_A}{dX}\right)}{\left(\frac{\omega^2}{v_A^2}-k_Z^2\right)\left(\frac{\omega^2}{v_A^2}-k_Z^2-k_Y^2\right)v_A^3} + \frac{1}{B_0}\frac{dB_0}{dX}\right\}\frac{dE_{1Y}}{dX} + \left(\frac{\omega^2}{v_A^2}-k_Z^2-k_Y^2\right)E_{1Y} = 0, \quad (3)$$

$$E_{1X} = \frac{ik_Y\frac{dE_{1Y}}{dX}}{\left(\frac{\omega^2}{v_A^2}-k_Z^2-k_Y^2\right)}, \quad (4)$$

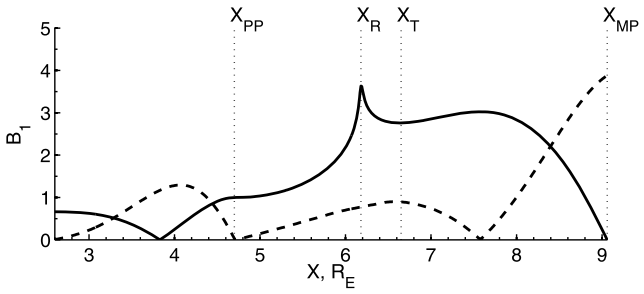

Figure 2. A time independent solution of the ideal MHD wave equation, for a frequency of 16 mHz, with $n = 2$. Magnetic field perturbations are shown in the X (solid) and Z (dashed) directions.

where $v_A = B_0/(R_E\sqrt{\mu_0\rho_0})$ is the Alfvén speed in Earth radii per second. In Cartesian coordinates, k_Y is equivalent to the azimuthal m number. All distances are in Earth radii (R_E), wave numbers are in radiansR_E^{-1}, and speeds are in R_E s^{-1}. In order to avoid a problematic singularity in (3) and (4) at $\omega^2/v_A^2 - k_Z^2 - k_Y^2 = 0$, the angular wave frequency ω is given an imaginary component. The negative damping factor $\gamma = \Im(\omega)/\Re(\omega)$ represents an irreversible loss of energy to the coupled field line resonances. The effect of this damping is to broaden a field line resonance without altering its location. The value of k_Z is taken to be $n \cdot \pi/5$, where $n = 1, 2, 3, \ldots$ and 5 is the normalized length of the field lines, following *Cheng et al.* [1998].

[21] After solving equations (3) and (4), the magnetic field perturbation is found using the Maxwell-Faraday equation:

$$\nabla \times \mathbf{E_1} = -\frac{\partial \mathbf{B_1}}{\partial t}. \tag{5}$$

[22] Thus, the magnetic field perturbation in the X direction is proportional to the electric field perturbation in the Y direction and vice versa.

[23] A numerical solution is presented in Figure 2, for magnetic field corresponding to the equatorial plane of a dipole ($B_0 \propto 1/X^3$), with the adjustable Alfvén speed profile utilized by *Cheng et al.* [1998], shown in Figure 3. The parameter values used in this solution are $P = 4.7$, $Q = 4.7$, $R = 7.37$, $v_{A0} = 0.0387$, with $\omega = 16 \times 10^{-3} \cdot 2\pi$, $\gamma = -0.0022$, $k_Z = 2 \cdot \pi/5$, and $k_Y = 0.5$. The Alfvén speed at the plasmapause, v_{A0}, and the parameter R, have been chosen such that an 8 mHz field line resonance will occur at 6.18 R_E, in accordance with observations of phase reversal in magnetometer data [*Menk et al.*, 2001].

[24] Without azimuthal boundaries the choice of k_Y seems arbitrary and, in reality, would be determined by the propagation of a solar wind pressure front along the magnetopause. Here we have chosen a value of 0.5 radians R_E^{-1}, equivalent to an m number of 3.5 at $X = 7$ R_E, which is not unreasonable.

[25] At the magnetopause the boundary conditions require that the electric field, and therefore the magnetic field perturbations in the X and Y directions, are zero. However, B_{1Z}, representing equatorially symmetric compressions and rarefactions of the magnetic field, is not zero. This is the means of energy transfer from solar wind pressure variations to the cavity mode waves.

[26] In the WKB approximation, $(\omega^2/v_A^2 - k_Z^2 - k_Y^2)^{1/2}$ can be thought of as the variable wave number $k_X(X)$. A turning point, X_T, is found in B_{1X}, where $k_X(X) = 0$. In our solution $X_T = 6.65$. Earthward of this point the cavity mode decays before resonance with field line oscillations occur at X_R. Across the field line resonance, which is centered on $k_Z = \omega/v_A$, there is a phase reversal in the toroidal component, B_{1Y}.

[27] Beyond X_R the cavity mode continues to decay until a second turning point is met. For an Alfvén speed profile proportional to $1/X$, the second turning point is located at $X_T/\sqrt{2}$, where $k_X(X) = i\omega/v_A$. In the absence of a plasmapause all three components have local minimum at the second turning point, where B_{1Y} and B_{1Z} are zero, but B_{1X} is non-zero and finite. Here, the magnetospheric cavity mode can efficiently couple to that of the plasmaspheric cavity, at the plasmapause, X_{PP}. The solution within the plasmaspheric cavity has an antinode in B_{1X} and nodes in B_{1Y} and B_{1Z} at the plasmapause, where neglecting damping $k_X(X)$ is once again real due to the lower Alfvén speed.

[28] The distance from, for example, the turning point X_T to the closest possible position of the magnetopause X_{MP} may be estimated using the phase integral equation:

$$\phi_n = \int_{X_T}^{X_{MP}} k_X(X)\, dX - (l - 1/4)\pi = 0, \tag{6}$$

where l is an integer.

[29] When the azimuthal wave number is not exactly zero, time independent solutions are available only for a plasmapause of zero thickness, indicating that a thin plasmapause is important for standing wave longevity in the combined plasmaspheric and magnetospheric cavity. Satellite observations [e.g., *Chappell et al.*, 1970] have shown that, during high *ap* index, the plasmapause is characterized by a fall in ion density of approximately three orders of magnitude in as little as 0.2 R_E. At low *ap* index the same ion density change typically occurs over a radial distance exceeding 1 R_E. Thus, we may expect that events are more likely at times of high *ap* index.

[30] The plasma density and the azimuthal wave number k_Y combine to determine a location of the second turning

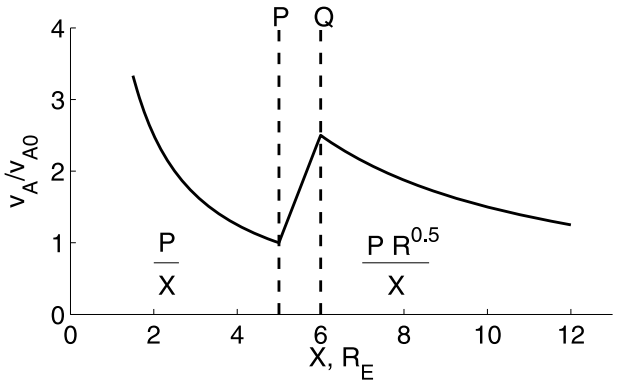

Figure 3. The adjustable Alfvén speed profile. Shown with $R = 9$, $P = 5$, and $Q = 6$. P and Q define the plasmapause, while v_{A0} is the Alfvén speed at P.

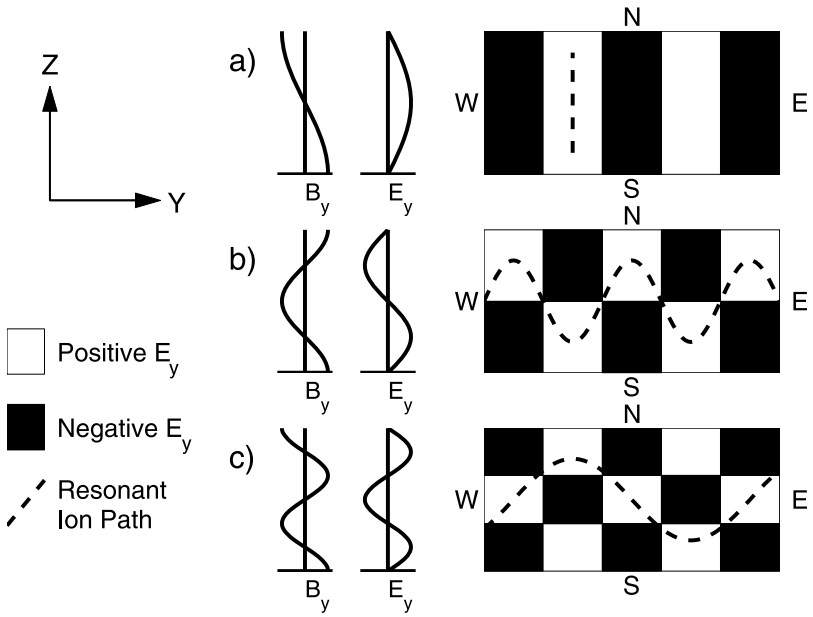

Figure 4. Illustration of the resonance condition (after *Southwood and Kivelson* [1982]). (a) $N = 0$, (b) $N = 1$, and (c) $N = 2$. The dashed lines represent the ion motion in the rest frame of the wave.

point in the magnetosphere that matches the location of the plasmapause. The magnetospheric plasma density, azimuthal wave number and plasmapause location have unique relationships with activity and local time. It is therefore expected that there will be a geomagnetic/solar activity dependence on the MLT of high *m* number observations. However, in order to establish relationships between such variables it would be necessary to abandon the Cartesian model, and fixed wave numbers, in favor of a more realistic geometry, which is beyond the scope of this paper.

[31] In summary, the simple box model provides estimates of the L-shell of phase-reversal for each cavity mode harmonic (utilized in section 4.2), predicts enhanced occurrence rates for a thin plasmapause, indicated by a high *ap* index, and predicts that there is likely to be an activity dependence on the MLT of events (explored in section 4.3).

3.3. Particle-Wave Resonance

[32] A charged particle drift-bouncing in the magnetosphere is able to resonate with a toroidal MHD wave when the *resonance condition* is met:

$$\omega - m\omega_d = N\omega_b \tag{7}$$

[*Southwood et al.*, 1969], where m is the azimuthal wave number, ω is the angular frequency of the wave, and ω_d and ω_b are the drift and bounce angular frequencies of the particle, respectively. N is the *resonance order*, an integer that may be positive, negative, or zero. A graphical representation of the resonance condition is given in Figure 4. Figures 4a, 4b, and 4c show the trajectories of an ion in resonance with the $N = 0$, 1, and 2 modes, respectively, in the rest frame of the wave.

[33] In a process known as Landau damping, drift-bouncing charged particles with slightly less energy than required for resonance will take energy from the wave, regardless of the direction of their motion around Earth. Conversely, in inverse-Landau damping, particles with slightly more energy than required for resonance will transfer energy to the wave.

[34] The proton drift [*Chisham*, 1996] and bounce [*Glassmeier et al.*, 1999] angular frequencies, in the Earth's rotating reference frame, are

$$\omega_d = \frac{EL^2}{B_s R_E} - \frac{6WL(0.35 + 0.15\,\sin(\alpha))}{B_s R_E^2}, \tag{8}$$

$$\omega_b = \frac{\pi\sqrt{W}}{\sqrt{2m_p}LR_E(1.3 - 0.56\,\sin(\alpha))}, \tag{9}$$

where L is the L-shell of the proton and W is its energy in eV, B_S is the equatorial magnetic field strength at the surface of Earth, α is the equatorial pitch angle of the proton, E is the magnetospheric electric field and m_p is the proton mass.

[35] We are concerned with resonance at the L value of the ARIES riometer, near geosynchronous orbit. Here, following *Baddeley et al.* [2002], equations (8) and (9) reduce to

$$\omega_d \approx C_1 + C_2 W, \tag{10}$$

$$\omega_b \approx \sqrt{C_3 W}, \tag{11}$$

where $C_1 = 7.7 \times 10^{-6}$, $C_2 = -1.44 \times 10^{-8}$, and $C_3 = 2.89 \times 10^{-7}$.

3.4. Combining Landau and Inverse-Landau Damping

[36] Protons accelerated by Landau damping will form a bump on the tail of their energy distribution functions. When the driving wave ceases, the bump-on-tail energy

becomes unstable to inverse-Landau damping, and the generation of a secondary MHD wave can occur. Combining equations (7)–(9), we find that a secondary wave has one of two degrees of freedom determined by the energy of the bump-on-tail particles; that is, the wave frequency and *m* number of a secondary wave are not fixed, but are dependent.

[37] For any particular frequency and *m* number of a driving wave, there will be a linear relationship between frequency and *m* number of all possible secondary waves. Considering equation (7), for both a driving and secondary wave in resonance with a common ion energy, we obtain the general linear relation

$$\omega_S = m_S\,\omega_d + \frac{N_S}{N_D}(\omega_D - m_D\,\omega_d), \tag{12}$$

where the D and S subscripts refer to the driving and secondary waves, respectively. If the properties of the driving wave are known, the proton angular drift frequency, ω_d, may be determined using equations (7)–(9) and substituted into equation (12) to reveal the possible parameters of a secondary wave. Thus, at geosynchronous orbit,

$$\omega_S = \frac{m_S}{m_D}\omega_D + \left(\frac{m_S}{m_D}N_D - N_S\right) \times \left[\frac{N_D C_3}{2m_D C_2} - \sqrt{\left(\frac{N_D C_3}{2m_D C_2}\right)^2 - \frac{C_3}{C_2}\left(C_1 - \frac{\omega_D}{m_D}\right)}\right]. \tag{13}$$

[38] On the basis of our hypothesis that many of the observed high *m* number waves are a product of resonances, driven by cavity-like wave modes, we look at the case of a large scale, i.e., small *m* number, driving wave. As $m_D \to 0$, equation (13) becomes

$$\omega_S(m_D \to 0) = m_S\left[C_1 + \frac{C_2}{C_3}\left(\frac{\omega_D}{N_D}\right)^2\right] + N_S\frac{\omega_D}{N_D}. \tag{14}$$

3.5. Resonance Orders

[39] The resonance orders N_D and N_S are integers, including negative values and zero. Since ω and ω_b are by definition positive, some values of *N* are not always possible, depending on the azimuthal direction of the wave (positive or negative *m*) and the azimuthal drift direction of the charged particle (positive or negative ω_d). Generally, smaller values of *N* produce more strongly coupled resonances, with $N = 0$ being the Cerenkov resonance. *N* must be nonzero and positive for eastward propagating MHD waves in resonance with protons. This is also the case with cavity mode-like waves, where the low azimuthal wave numbers would require unrealistically high particle energies for $N = 0$. However, westward traveling waves may resonate with $N_S = \ldots, -2, -1, 0, 1, 2, \ldots$ and would therefore present a more complicated picture.

[40] It can be seen from Figure 4 that the shear Alfvén harmonic *n* is related to the resonance order by $n = N + 1$. Since $N = 1$ is expected to be the strongest resonance for cavity mode waves, $n = 2$ is used in our model solution (section 3.2).

3.6. Modulation of Precipitation

[41] The capability of magnetospheric ULF waves to modulate electron precipitation has been well established via observation [e.g., *Spanswick et al.*, 2005]. *Coroniti and Kennel* [1970] (see also *Haugstad* [1975]) suggested that the magnetic pulsation modulates the growth rate of whistler mode wave turbulence. Since these waves drive pitch angle diffusion via Doppler-shifter cyclotron resonance, the electron precipitation is modulated. *Nosé et al.* [1998] offered an alternative mechanism whereby electrons are accelerated due to the parallel electric field of a kinetic Alfvén wave. For this study the actual mechanism that operates is unimportant; it is enough that the modulation of electron precipitation is occurring.

4. ARIES Results

[42] The times of all of the detected high *m* number wave events are displayed in Figure 5. There is clearly a relationship between solar wind activity and observations of high *m* number waves. Since they require a source of protons for drift-bounce resonance and electrons for precipitation, it is not unexpected that observations tend to occur following substorm activity, when charged particles are drifting toward the dayside magnetosphere. If high *m* waves are not observed, it could be due to a lack of particles rather than an indication that magnetic pulsations are absent.

[43] In analyzing data from ARIES, *cross-power*, the Fourier transform of the cross-correlation function, and *cross-phase*, the frequency dependent phase difference, are calculated for pairs of equilatitudinal beams. The definition of cross-power is identical to the product of the two Fourier transforms, where one of them has been complex conjugated. Forty-two beam pairs located close to the zenith are employed.

[44] Azimuthal wave numbers are determined from the cross-phase and the known ARIES beam spacing, with an assumption that peak absorption is at an altitude of 90 km. Results from beam-pairs are averaged to reduce error and searched for wave-like structures with frequencies between 0.3 and 17 mHz. Neighboring beams are paired when analyzing large *m* number events, whereas to improve accuracy neighbor-but-one beam pairs are chosen for *m* numbers below 250. ARIES is aligned geographically; although it is not feasible to pair beams of the same geomagnetic latitude without severe aliasing due to a wide beam separation, the effect of this rotation is expected to be, at most, a few percent in the calculated *m* numbers.

[45] Phase maps of two frequencies present during a typical event on 17 January 2007 are shown in Figure 6. These illustrate the relative phase of each beam, in radians, filtered at a specific frequency. The zero point is arbitrary. For the same event, unfiltered data from five neighboring ARIES beams and the X (north) components of two nearby magnetometers are given in Figure 7. Clear phase differences are visible across the ARIES beams. The magnetometers at Tromsø (69.66°N, 18.94°E) and Andenes (69.30°N, 16.03°E) are not capable of detecting waves with small spatial scales, as they effectively integrate over a wide area of sky; instead they respond to a concurrent 7–8 mHz large-scale wave, which is observed between 05:15 UT and 06:00 UT and thought to be the driver of the event. A similar integration

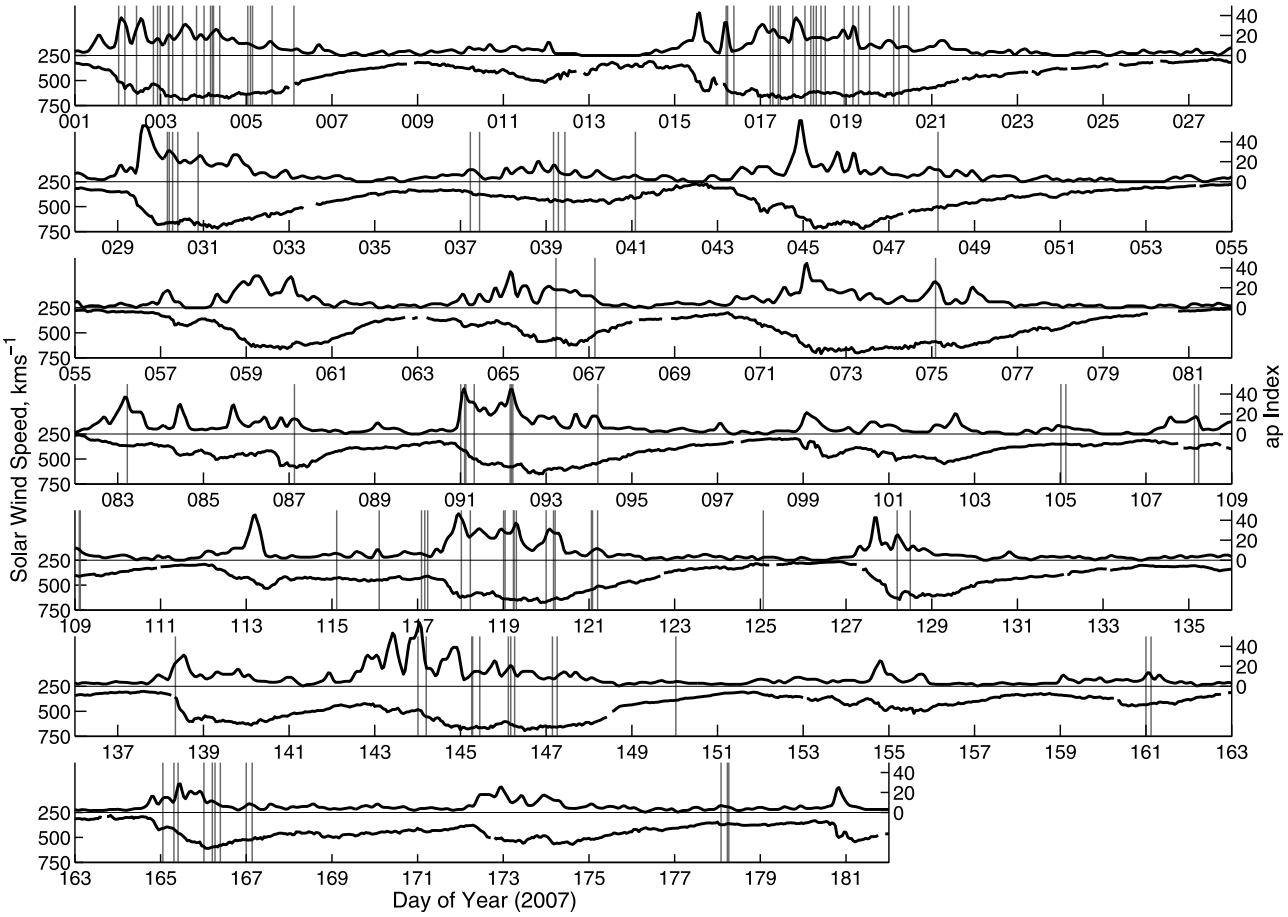

Figure 5. Occurrences of high azimuthal wave number ($|m| \geq 60$) events in ARIES, during the first 6 months of 2007.

effect is seen in the westernmost riometer beam, where the dip in received power at 05:24 UT is smoothed due to the larger beam size.

4.1. Dispersion Relation of High *m* Number Waves

[46] The dispersion relations of high *m* number waves observed by ARIES between 7.5 and 14 MLT (Figure 8) have distinct features consistent with secondary waves driven by large-scale MHD waves through Landau followed by inverse-Landau damping of the magnetospheric proton population, as described in section 3.4. All have ionospheric velocities of less than 1 km s^{-1}.

[47] The frequency values of driving waves used in equation (14) for the calculation of the fitted lines are $f_D/N_D = 0.8, 8, 11.5, 16, 23, 30.5, 38.5$ mHz. It is not possible to differentiate between resonance orders N_D since it is the value of f_D/N_D that determines the energy of the resonant protons, and the dispersion relation of the secondary waves. The same is not generally true of N_S, for which there are events of $N_S = 1$ and $N_S = 2$. Consequently, events associated with $f_D/N_D = 8$ and 11.5 mHz, for example, could be 16 and 23 mHz cavity modes, respectively, with $N_D = 2$.

[48] Lower frequencies f_D and higher resonance orders N_D and N_S are capable of producing higher *m* number secondary waves. For an $f_D = 16$ mHz driving wave, the N_D 1 N_S 1 case may generate up to $m \sim 200$ waves, whereas the N_D 2 N_S 1 and N_D 1 N_S 2 cases are capable of producing waves of up to $m \sim 400$. The highest *m* number observed (380) is attributed to N_D 1 N_S 2.

[49] An *m* number of 380 corresponds to an azimuthal wavelength (λ_{Az}) of 697 km at geostationary orbit and 37.4 km in the ionosphere above ARIES. Given the invariance of $v_\perp^2/B$ over the bounce period of a charged particle in a dipole field, it can be shown that the ratio of the azimuthal wavelength to the Larmor radius (λ_{Az}/ρ) is smallest in the equatorial plane. Drift-bounce resonance, with $N \neq 0$, strongly favors particles of small equatorial pitch angle [*Southwood and Kivelson*, 1982; *Baddeley et al.*, 2002]. Assuming a pitch angle of 10°, for a resonant proton in the $m = 380$ event, provides a ratio of $\lambda_{Az}/\rho \approx 15$, in the equatorial plane.

[50] Three data points below 1 mHz do not appear to match the linear relations for cavity mode frequencies. It could be that the same (Landau followed by inverse-Landau damping) mechanism is acting on a lower frequency group of magnetospheric waves, for example, the slow magnetosonic (SMS) oscillations described by *Leonovich et al.* [2006]. The SMS waves resonate with fundamental frequencies between 0.1 and 1 mHz, and have amplitudes that fall rapidly upon approaching the ionosphere. This implies that the ionosphere cannot absorb a significant amount of the wave energy and led *Leonovich et al.* [2006] to conclude: "SMS

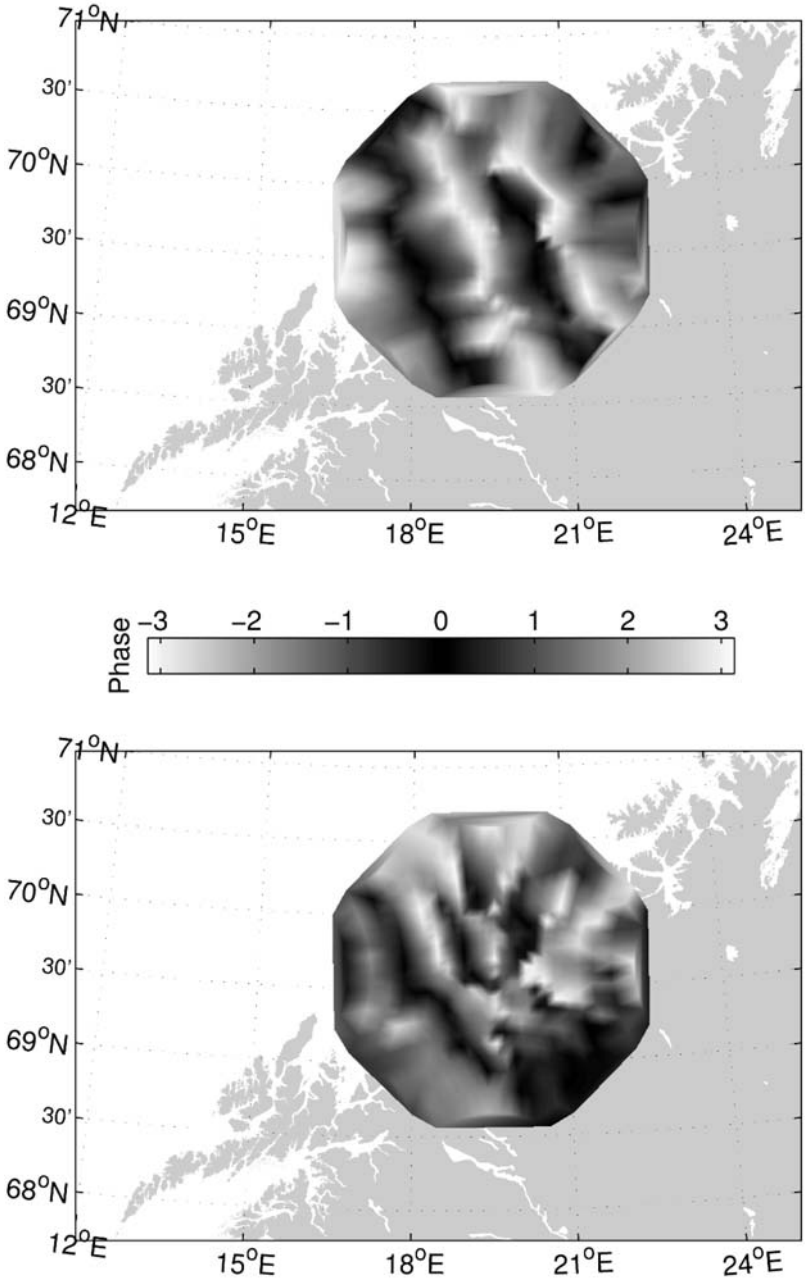

Figure 6. Phase maps of 17 January 2007 05:30 UT. (top) 3.2 mHz, m = 120. (bottom) 5.7 mHz, m = 320.

wave damping in the magnetosphere must be caused by other mechanisms, probably by their resonant interaction with the background plasma particles." Figure 8 includes a linear secondary wave function calculated for a 0.8 mHz large-scale driving wave. However, it should be noted that the fit of few data points is improved following this inclusion.

[51] Eastward high m wave events are observed in reduced numbers as early as 2.5 MLT, but those occurring before 7.5 MLT do not to fit the dispersion relation functions of the dayside events, and are excluded from Figure 8. This is to be expected, due to the MLT variation in the size of the magnetospheric cavity away from the dayside, which alters the frequencies of cavity modes and, subsequently, the dispersion relation functions. Additionally, pulsations in the flanks of the magnetosphere driven by the Kelvin-Helmholtz instability are predicted to have similar frequencies (5–10 mHz), with varying m numbers (typically $m \sim 15$) [*Claudepierre et al.*, 2008]. If such waves are driving sources in the generation of high m waves, either by the mechanism under consideration or otherwise [e.g., *Allan et al.*, 1997], evidence in the dispersion relations of any secondary waves will be difficult to find. Analysis is restricted to eastward waves observed around local noon, a stagnation point for the solar wind, where velocity shear is minimized, and clear patterns in the dispersion relations are found. It should be noted that although the waves have velocities in the eastward direction, the events themselves do not propa-

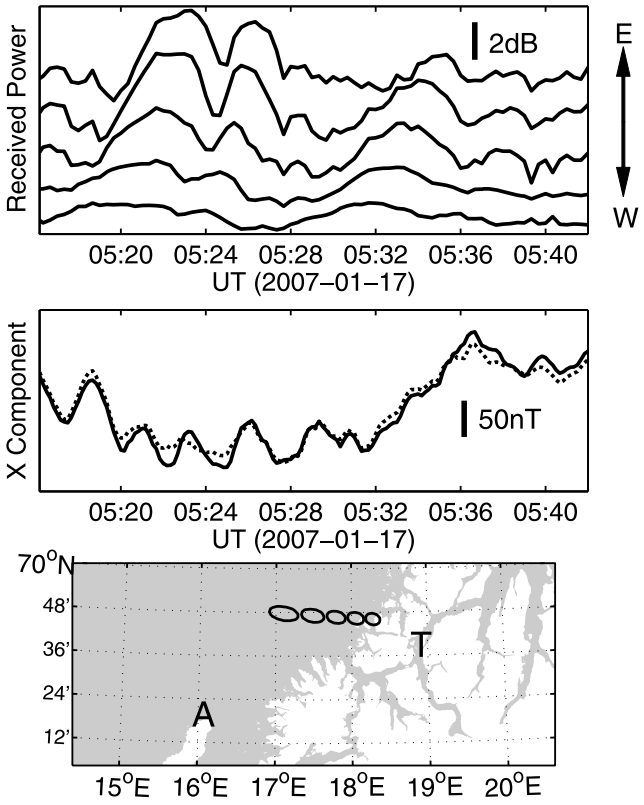

Figure 7. Unfiltered data from the event of 17 January 2007 (see Figure 6). (top) ARIES received power from five individual neighboring beams. (middle) Tromsø (solid) and Andenes (dotted) X component magnetometer data. (bottom) Map showing the locations of the five ARIES beams (projected to 90 km altitude), and the Tromsø and Andenes magnetometers.

gate. The wave is generated and decays within a fixed MLT, evidenced by observations on successive days.

4.2. Phase Reversal at Field Line Resonance

[52] An event on 18 May 2007 (Figure 9) displays an apparent phase reversal between the northern and southern halves of the ARIES field of view. This is especially clear in the east, where an imagined straight line following a northern crest would continue along a southern trough, and vice versa. Such a phase reversal is expected at the L value of a field line resonance, theoretically (see section 3.2), and as a well-known feature of magnetometer FLR observations. Physically, it is interpreted as a reversal in the bouncing phase of resonant ions, spread over a finite radial distance due to damping and a finite electric field perturbation.

[53] The frequency and azimuthal wave number of this event suggest a cavity mode driving wave of f_D/N_D = 11.5 mHz, for which the box model calculation, calibrated by magnetometer FLR observation, predicts a phase reversal centered at $X = 6.44\ R_E$. Using the Tsyganenko T01 model [*Tsyganenko*, 2002a, 2002b], with suitable inputs for the time of the event, agreement is found in tracing the magnetic field from the ionosphere directly above ARIES to an equatorial distance of 6.52 R_E.

4.3. Location of High *m* Number Waves

[54] It was discussed in section 3.2 that cavity mode waves depend on various magnetospheric parameters. Of particular importance are likely to be the Alfvén speed profile, and the location and thickness of the plasmapause. In Figure 5, a correlation is found between times of enhanced *ap* index and solar wind speed, and the observations of high *m* number events. Although this could be due to an increase in particle flux following substorm activity, a heightened *ap* index is indicative of a thin plasmapause, conducive to the existence of cavity modes. Furthermore, the events occur exclusively with $ap \geq 5$, while between 1 January 2007 and 30 June 2007, the period from which the data set is taken, 48.5% of *ap* values are below 5. This could be suggestive of a limit in plasmapause thickness, above which the mechanism cannot operate.

[55] Following *Chappell et al.* [1970], a basic estimate for the plasmapause location may be obtained from the maximum *ap* index of the preceding 12 h. In Figure 10, the distribution of the events in MLT is plotted against this estimated plasmapause location, for which a correlation is found.

[56] It is probable that the coherence of dayside cavity mode waves over a range of MLT is key in the formation of a significant bump on the tail of the proton energy distribution. High *m* number CNA pulsations with approximately identical properties are often observed on consecutive days at the same MLT, indicating a long-lived nature. In conjunc-

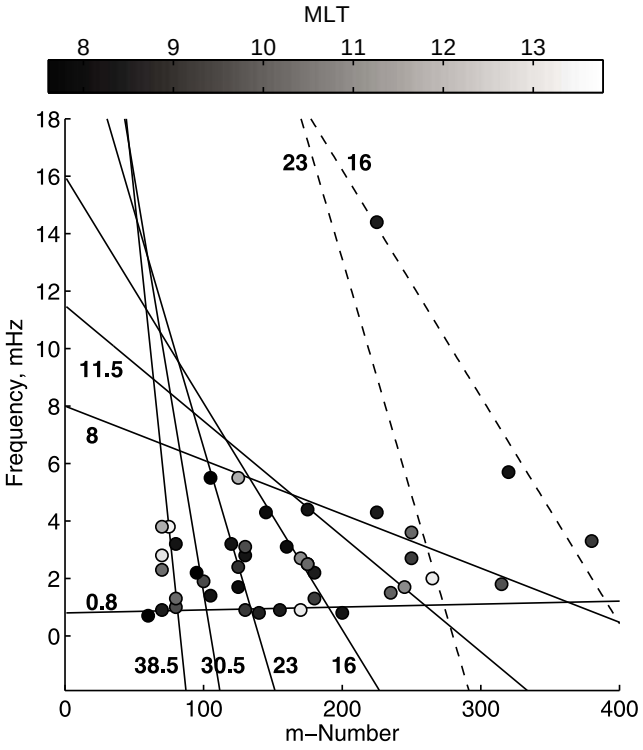

Figure 8. The dispersion relation of wave structures found in ARIES with $m \geq +60$, between 7.5 and 14 MLT. Solid lines are $N_S = 1$ resonance and dashed are $N_S = 2$. The adjoined numbers are the values of f_D/N_D, in mHz, used in the equation of each line.

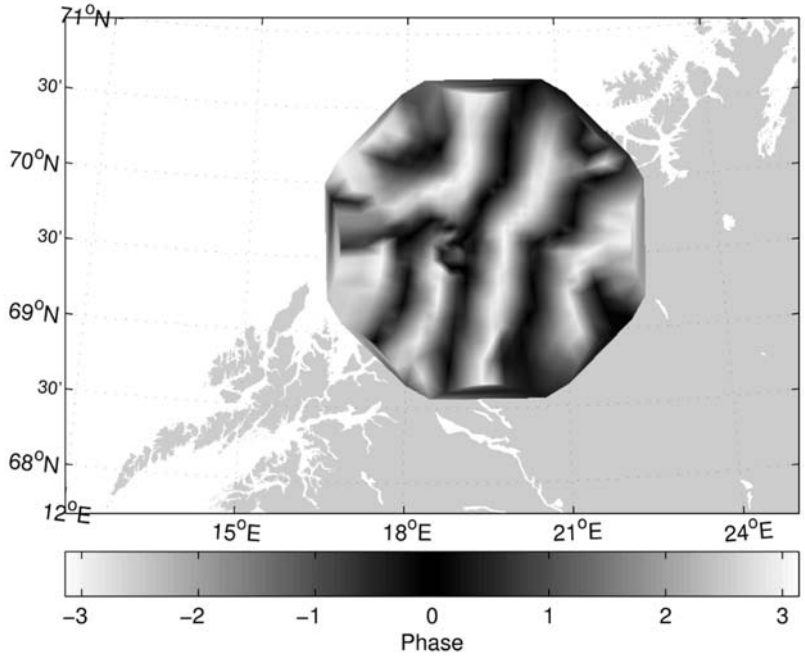

Figure 9. The phase map of an event on 18 May 2007 08:20 UT, associated with the resonant cavity mode of frequency f_D/N_D = 11.5 mHz.

tion with the typically small (~1 h) MLT range, this suggests that the local time distribution may be determined at a stage after the Landau damping of cavity modes, perhaps at the location of a threshold in the number of electrons available for modulated precipitation. We can further speculate that beyond the location of this threshold, the loss rate of bump-on-tail energy from the westward drifting proton distribution to the modulated electron precipitation may determine the local time extent of the pulsations.

[57] In Figure 11a, the normalized power of detected waves is given as a function of MLT, and in Figure 11b as a function of X, the radial distance in R_E, traced for each event along the magnetic field, using the Tsyganenko magnetic field model [*Tsyganenko*, 2002a, 2002b]. It is not pos-

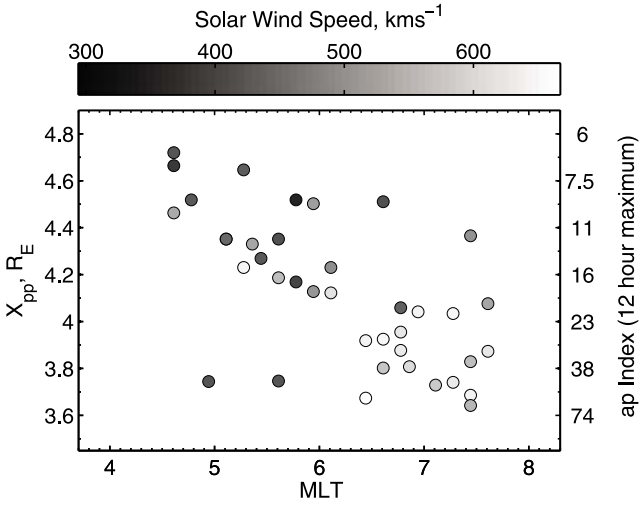

Figure 10. The effect of *ap* index and the corresponding estimated plasmapause position on the local time of high *m* number events. The correlation coefficient is −0.69.

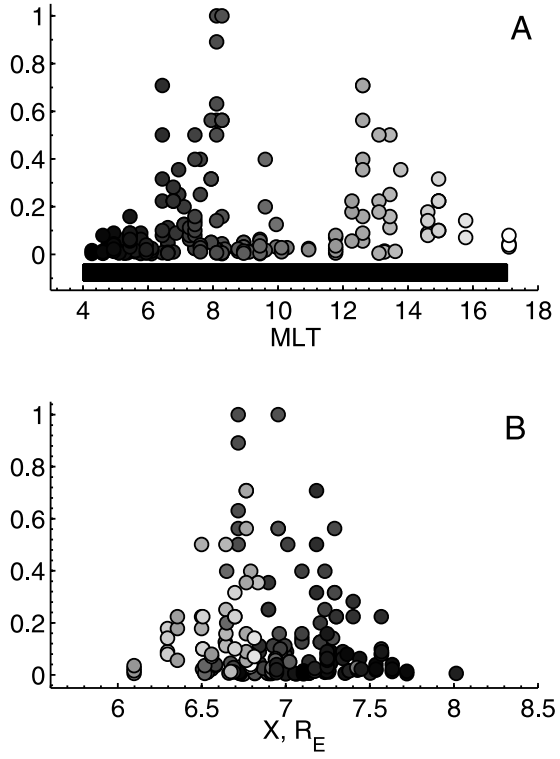

Figure 11. (a) Normalized wave power versus MLT. (b) Normalized wave power as a function of radial distance. Shade represents MLT.

Table 1. Energy Values

Cavity Mode Frequency/N_D (mHz)	Resonant H^+ Energy (keV)
0.8	0.087
8	8.7
11.5	18
16	35
23	72
30.5	127
38.5	202

sible to separate local time variations in power from those of radial distance; however, a peak in the wave power is found where the riometer location is traced to 7 R_E, at 8 MLT and 12.5 MLT.

5. CAMMICE (MICS) Results

[58] The proposed mechanism makes a testable prediction of the proton energy distribution in the dayside magnetosphere. Positive gradient regions should commonly exist at discrete energy values corresponding to Landau damping of the magnetospheric cavity modes. These energy values are given in Table 1.

[59] Previously, *Baddeley et al.* [2002] conducted a survey of bumps-on-the-tails of proton energy distributions near geosynchronous orbit, using Polar CAMMICE data from 1996 through 2001. Positive gradient regions were found to exist predominantly between 05 and 14 MLT, with occurrence rates peaking above 40%. The explanation of this MLT distribution is quite straightforward: protons drift westward from the nightside injection region; on reaching the dayside magnetosphere, those near resonance are accelerated by Landau damping of cavity mode waves. They continue to drift westward into the morning sector, until the free energy in the distribution is lost to the inverse-Landau damping of secondary MHD waves.

[60] Figure 12 shows the occurrence rate of detected enhancements in the proton distribution function as a function of energy. The data are restricted to times when the Polar spacecraft is located within L values of 5–9 and MLT of 05–14.

[61] The authors suspect that enhancements occupying single energy channels are being flagged as bad data during the processing of CAMMICE data. Bad data values, for example following a loss of synchronization, should be independent of the ESA stepping pattern and therefore independent of energy channel. However, cases in which single channels are flagged are found to strongly favor those channels closest to the expected energies of the f_D/N_D = 11.5, 16 and 23 mHz resonances. At lower energies, corresponding to f_D/N_D = 8 mHz, enhancements occupy more than one of the logarithmically spaced energy channels and are more properly detected as bumps in the energy distribution function, seemingly unaffected by the CAMMICE quality control processing.

[62] For this reason, flagged data are included as positive detections of enhancements if the values in neighboring energy channels are valid.

[63] At energies above 70 keV, the widths of the energy channels are significantly greater than their spacing, and the detection of enhancements in the distribution becomes problematic.

6. Discussion and Conclusion

[64] The primary result of this study is in the dispersion relations of dayside, high *m* number, eastward propagating waves (Figure 8). These show clear structure, matching well with functions expected from cavity mode (i.e., large-scale) sources, with frequencies of 8, 11.5, 16, 23, 30.5, and 38.5 mHz. Several of these frequencies appear in previous studies. *Yumoto et al.* [1994] reported global magnetometer observations of cavity-like oscillations at 15.5, 25, and 31 mHz, following interplanetary impulses. *Sibeck et al.* [1989] observed ringing at a period of 2 min (8.3 mHz) in the outer magnetospheric magnetic field, following a step function increase in solar wind pressure. Furthermore, quasi-monochromatic 2 min oscillations in the magnetic field, ion number density, temperature and velocity in the dawnside magnetosphere have been encountered by the Equator-S spacecraft [*Rae et al.*, 2007].

[65] Spectral analysis of ringing within a model magnetosphere, following a solar wind pressure pulse [*Lee et al.*, 2004], provided similar frequencies: 8, 16–23, 30, 40 mHz, and so on. *Claudepierre et al.* [2009] conducted global solar wind-magnetosphere 3-D MHD simulations and reported a fundamental cavity mode frequency close to 10 mHz, whereas *Fujita and Itonaga* [2003] calculate an eigenmode frequency of 14 mHz at dawn and 18 mHz at dusk, for resonance within the plasmaspheric cavity.

[66] It becomes increasingly clear that the cavity mode frequencies inferred herein are commonplace in the dayside magnetosphere, with the probable exception of 11.5 mHz, which is taken to be the 23 mHz cavity mode, resonating with N_D = 2.

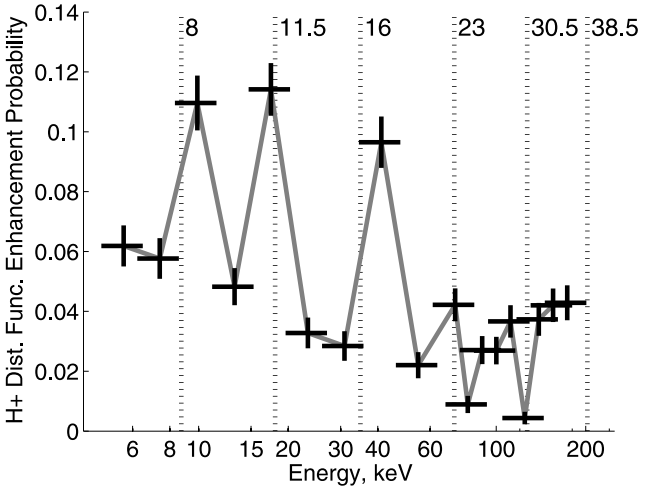

Figure 12. The occurrence rate of detected enhancements in the proton distribution function. The data set is restricted to the times when Polar is within $5 < L < 9$ and 5 MLT < 14. Dotted lines indicate the energies of resonant protons for each cavity mode frequency (labels are f_D/N_D in mHz). Horizontal bars represent energy bin widths and vertical bars indicate the standard error in the mean.

[67] The well-known global modes of 1.3, 1.9, 2.6, and 3.4 mHz [*Samson et al.*, 1991; *Samson and Rankin*, 1994] are notably absent. There is a growing opinion that such frequencies are too small to be dayside magnetospheric cavity modes, and may be forced oscillations at frequencies present in the solar wind [*Leonovich and Mazur*, 2001; *Eriksson et al.*, 2006, and references therein]. Simulations of less than 5 mHz fluctuations in the solar wind dynamic pressure have been found not to excite cavity modes, but undergo evanescent decay earthward of the magnetopause [*Claudepierre et al.*, 2009]. If waves of these frequencies exist with the capacity to generate significant bumps on the tail of the proton distributions, secondary waves could be generated with *m* numbers beyond the observable limit of ARIES. At $f_D/N_D < 2$ mHz, m_S is not constrained, and finite Larmor radius effects should be considered. In such cases it could be that destabilized Alfvén modes with azimuthal wavelengths of double the Larmor radius are favored [see *Dettrick et al.*, 2003].

[68] In a detailed case study of a single dayside event using the CUTLASS HF radars, *Yeoman and Wright* [2000] split the event duration into three intervals. During the first interval, Fourier components of 5.7 and 16 mHz were observed, with low azimuthal wave numbers of $m = 6 \pm 3$. The second interval contained a dominant 3.8 mHz component, with $m = -35 \pm 6$, and the final interval was dominated by a 14.3 mHz wave, also with $m = -35 \pm 6$. Our study has neglected westward (negative *m* number) waves, because the numerous and varied modes of resonance would not be expected to show clear dispersion relation patterns. However, *Yeoman and Wright* [2000] inferred the proton energies that would be required to drive the observed westward waves through drift-bounce resonance interactions. These were 47 ± 10 keV for the second interval and 34 ± 10 keV for the third. Agreement is found with the 35 keV proton energy derived in this paper for a 16 mHz cavity mode (low *m* number) wave, which may have been directly observed during the first interval of the event.

[69] A possible reason why this mechanism has been previously overlooked can be found in the early theory of drift-mirror instability [*Hasegawa*, 1969], in which Landau damping is assumed to be prevented by the lack of parallel electric fields. Clearly, this is not the case where drift-bounce resonance exists between waves and a particle population. This is not to say however that other mechanisms, such as pressure anisotropy, do not play a role in the acceleration of particles and subsequent generation of MHD waves.

[70] Further work needs to be done with regard to the data from CAMMICE (Polar), before it can be claimed that enhancements in the magnetospheric proton distribution function occur at energies corresponding to the cavity mode frequencies, but the early results appear promising.

[71] The sum of evidence suggests that the high *m* number waves observed in the morning sector cosmic noise absorption are caused by electron precipitation modulation by drift-bounce resonant toroidal MHD waves, which are generated by cavity mode waves through a process of Landau damping followed by inverse-Landau damping with the magnetospheric proton population.

[72] **Acknowledgments.** ARIES development was funded by the UK's Particle Physics and Astronomy Research Council (PPARC), now the Science and Technology Facilities Council (STFC). Solar wind data is courtesy of the OMNI dataset [*King and Papitashvili*, 2005]. Polar orbital and CAMMICE data was obtained from CDAWEB (http://cdaweb.gsfc.nasa.gov/), with thanks to Theodore Fritz, PI of the CAMMICE (MICS) instrument.

[73] Amitava Bhattacharjee thanks Viacheslav Pilipenko and another reviewer for their assistance in evaluating this paper.

References

Acuña, M. H., et al. (1995), The global geospace science program and its investigations, *Space Sci. Rev.*, *71*, 5–21.

Allan, W., et al. (1997), Large *m* waves generated by small *m* field line resonances via the nonlinear Kelvin-Helmholtz instability, *J. Geophys. Res.*, *102*, 19,927–19,934.

Baddeley, L. J., et al. (2002), Morning sector drift-bounce resonance driven ULF waves observed in artificially induced HF radar backscatter, *Ann. Geophys.*, *20*, 1487–1498.

Chappell, C. R., et al. (1970), A study of the influence of magnetic activity on the location of the plasmapause as measured by OGO 5, *J. Geophys. Res.*, *75*, 50–56.

Cheng, C. C., et al. (1998), Evidence of the coupling of a fast magnetospheric cavity mode to field line resonances, *Earth Planets Space*, *50*, 683–697.

Chisham, G. (1996), Giant pulsations: An explanation for their rarity and occurrence during geomagnetically quiet times, *J. Geophys. Res.*, *101*, 24,755–24,763.

Claudepierre, S. G., et al. (2008), Solar wind driving of magnetospheric ULF waves: Pulsations driven by velocity shear at the magnetopause, *J. Geophys. Res.*, *113*, A05218, doi:10.1029/2007JA012890.

Claudepierre, S. G., et al. (2009), Magnetospheric cavity modes driven by solar wind dynamic pressure fluctuations, *Geophys. Res. Lett.*, *36*, L13101, doi:10.1029/2009GL039045.

Coroniti, F. V., and C. F. Kennel (1970), Electron precipitation pulsations, *J. Geophys. Res.*, *75*, 1279–1289.

Dettrick, S., et al. (2003), Kinetic theory of geomagnetic pulsations: 4. Hybrid gyrokinetic simulation of drift-bounce resonant excitation of shear Alfvén waves, *J. Geophys. Res.*, *108*(A4), 1150, doi:10.1029/2002JA009650.

Eriksson, P. T. I., et al. (2006), A statistical correlation of Pc5 pulsations and solar wind pressure oscillations, *Adv. Space Res.*, *38*, 1763–1771.

Fujita, S., and M. Itonaga (2003), A plasmaspheric cavity resonance in a longitudinally non-uniform plasmasphere, *Earth Planets Space*, *55*, 219–222.

Glassmeier, K. H., et al. (1999), Concerning the generation of geomagnetic giant pulsations by drift bounce resonance ring current instabilities, *Ann. Geophys.*, *17*, 338–350.

Grill, M., et al. (2003), A new imaging riometer based on mills cross technique, paper presented at 7th International Symposium on Communication Theory and Applications, Ambleside, U. K.

Hasegawa, A. (1969), Drift mirror instability in the magnetosphere, *Phys. Fluids*, *12*, 2642–2650.

Haugstad, B. S. (1975), Modification of a theory of electron precipitation pulsations, *J. Atmos. Terr. Phys.*, *27*, 257–272.

Kikuchi, T. (1988), Eastward propagation of Pc4-5 range CNA pulsations in the morning sector observed with scanning narrow beam riometer at $L = 6.1$, *Geophys. Res. Lett.*, *15*, 168–171.

King, J. H., and N. E. Papitashvili (2005), Solar wind spatial scales in and comparisons of hourly wind and ACE plasma and magnetic field data, *J. Geophys. Res.*, *110*, A02104, doi:10.1029/2004JA010649.

Lee, D. H., et al. (2004), Effects of ionospheric damping on MHD wave mode structure, *Earth Planets Space*, *56*, e33–e36.

Leonovich, A. S., and V. A. Mazur (2001), On the spectrum of magnetosonic eigenoscillations of an axisymmetric magnetosphere, *J. Geophys. Res.*, *106*, 3919–3928.

Leonovich, A. S., et al. (2006), Magnetosonic resonance in a dipole-like magnetosphere, *Ann. Geophys.*, *24*, 2277–2289.

Menk, F. W., et al. (2001), Coordinated observations of forced and resonant field line oscillations at high latitudes, *ANARE Rep. Aust. Antarct. Div.*, *146*, 383–404.

Nosé, M., et al. (1998), Electron precipitation accompanying Pc 5 pulsations observed by the DE satellites and at a ground station, *J. Geophys. Res.*, *103*, 17,587–17,604.

Rae, I. J., et al. (2007), Equator-S observations of drift mirror mode waves in the dawnside magnetosphere, *J. Geophys. Res.*, *112*, A11203, doi:10.1029/2006JA012064.

Samson, J. C., and R. Rankin (1994), The coupling of solar wind energy to MHD cavity modes, waveguide modes, and field line resonances in the Earth's magnetosphere, in *Solar Wind Sources of Magnetospheric Ultra-Low-Frequency Waves*, *Geophys. Monogr. Ser.*, vol. 81, edited

by M. J. Engebretson, K. Takahashi, and M. Scholer, pp. 253–264, AGU, Washington, D. C.

Samson, J. C., et al. (1991), Magnetometer and radar observations of magnetohydrodynamic cavity modes in the Earth's magnetosphere, *Can. J. Phys.*, *69*, 929–937.

Senior, A., and F. Honary (2003), Observations of the spatial structure of electron precipitation pulsations using an imaging riometer, *Ann. Geophys.*, *21*, 997–1003.

Sibeck, D. G., et al. (1989), Solar wind dynamic pressure variations and transient magnetospheric signatures, *Geophys. Res. Lett.*, *16*, 13–16.

Southwood, D. J., and M. G. Kivelson (1982), Charged particle behavior in low-frequency geomagnetic pulsations: 2. Graphical approach, *J. Geophys. Res.*, *87*, 1707–1710.

Southwood, D. J., et al. (1969), Bounce resonant interaction between pulsations and trapped particles, *Planet. Space Sci.*, *17*, 349–361.

Spanswick, E., et al. (2005), Pc5 modulation of high energy electron precipitation: Particle interaction regions and scattering efficiency, *Ann. Geophys.*, *23*, 1533–1542.

Tsyganenko, N. A. (2002a), A model of the near magnetosphere with a dawn-dusk asymmetry: 1. Mathematical structure, *J. Geophys. Res.*, *107*(A8), 1179, doi:10.1029/2001JA000219.

Tsyganenko, N. A. (2002b), A model of the near magnetosphere with a dawn-dusk asymmetry: 2. Parametrization and fitting to observations, *J. Geophys. Res.*, *107*(A8), 1176, doi:10.1029/2001JA000220.

Wilken, B., et al. (1992), Magnetospheric ion composition spectrometer aboard the CCRES spacecraft, *J. Spacecr. Rockets*, *29*, 585–591.

Yeoman, T. K., and D. M. Wright (2000), ULF waves with drift resonance and drift-bounce resonance energy sources as observed in artificially-induced HF radar backscatter, *Ann. Geophys.*, *19*, 159–170.

Yumoto, K., et al. (1994), Global cavity mode-like and localized field-line Pc3-4 oscillations stimulated by interplanetary impulses (Si/Sc): Initial results from the 210° MM magnetic observations, in *Solar Wind Sources of Magnetospheric Ultra-Low-Frequency Waves*, *Geophys. Monogr. Ser.*, vol. 81, edited by M. J. Engebretson, K. Takahashi, and M. Scholer, pp. 335–344, AGU, Washington, D. C.

M. Beharrell, F. Honary, and A. J. Kavanagh, Department of Communication Systems, University of Lancaster, Lancaster LA1 4WA, UK. (m.beharrell@lancaster.ac.uk)